

Article

An All-Region State-of-Charge Estimator Based on Global Particle Swarm Optimization and Improved Extended Kalman Filter for Lithium-Ion Batteries

Xin Lai * , Wei Yi, Yuejiu Zheng * and Long Zhou

School of Mechanical Engineering, University of Shanghai for Science and Technology, Shanghai 200093, China; 13072182082@163.com (W.Y.); zhoulong925@126.com (L.Z.)

* Correspondence: laixin@usst.edu.cn (X.L.); yuejiu_zheng@163.com (Y.Z.); Tel.: +86-021-5527-5287 (X.L.)

Received: 29 October 2018; Accepted: 12 November 2018; Published: 14 November 2018



Abstract: In this paper, a novel model parameter identification method and a state-of-charge (SOC) estimator for lithium-ion batteries (LIBs) are proposed to improve the global accuracy of SOC estimation in the all SOC range (0–100%). Firstly, a subregion optimization method based on particle swarm optimization is developed to find the optimal model parameters of LIBs in each subregion, and the optimal number of subregions is investigated from the perspective of accuracy and computation time. Then, to solve the problem of a low accuracy of SOC estimation caused by large model error in the low SOC range, an improved extended Kalman filter (IEKF) algorithm with variable noise covariance is proposed. Finally, the effectiveness of the proposed methods are verified by experiments on two kinds of batteries under three working cycles, and case studies show that the proposed IEKF has better accuracy and robustness than the traditional extended Kalman filter (EKF) in the all SOC range.

Keywords: lithium-ion batteries; SOC estimator; parameter identification; particle swarm optimization; improved extended Kalman filter; battery management system

1. Introduction

Concerns about the impact of environmental degradation and the energy crisis have encouraged humans to develop new sustainable energy resources, and energy conversion and storage devices involving lithium batteries (LIBs), lead-acid batteries, nickel-cadmium batteries, fuel cells and supercapacitors, have become research hotspots [1–5]. Currently, LIBs have been regarded as the first choice for electric vehicles (EVs) because of their low self-discharge rate, high energy density, long lifespan and almost zero memory effect [6–9]. To ensure the safe operation of LIBs, an effective battery management system (BMS) was designed to provide monitoring and protection in EV applications [10,11]. One of the major functions of BMS is the real-time estimation of various battery states, such as state-of-charge (SOC), state-of-health [12] and state-of-energy [13]. For a BMS in EVs, one of the most important states is SOC, which indicates the remaining driving range. Therefore, accurate SOC estimation is of great significance to enhance the reliability and safety of EVs. In recent decades, SOC estimation techniques have been extensively reported by a number of researchers [14–16].

1.1. Review of SOC Estimation Approaches

The LIB is a dynamic nonlinear and time-varying system, and the SOC of a LIB cannot be measured directly. Thus, accurate SOC estimation is a cumbersome task [17]. In recent years, many studies have been devoted to developing methodologies for SOC estimation. Traditionally, frequently-used SOC estimation methods can be simply divided into two categories: non-model based methods and

model-based methods [15,18]. As a non-model based method, the coulomb counting method is easy to realize, however it suffers from the error accumulation problem caused by the initial value and current sensor errors [19]. For model-based methods, three key factors for obtaining an accurate SOC can be summarized, namely, a suitable model structure, matched model parameters and a robust estimation algorithm. In other words, the accuracy of the SOC estimation heavily depends on the battery model and estimator algorithm.

Due to a relatively simple mathematical structure and low computation burden, equivalent circuit models (ECMs) have become the most popular models utilized to describe the input/output behavior of LIBs through electrical circuits [20,21]. The commonly used ECMs are based on the RC networks with different orders. Obviously, the model structure and model parameters directly affect the model accuracy. Therefore, a model parameter identification algorithm is very important for improving the model accuracy. In existing studies, a variety of optimization algorithms have been used to identify model parameters of ECMs, such as the genetic algorithm (GA) [10], the particle swarm optimization (PSO) algorithm [22], and the least-squares method [23].

There is no doubt that the estimation algorithm is crucial to the SOC estimation accuracy. In the literature, several SOC estimation algorithms have been presented to improve the accuracy, reliability and robustness of estimation [24,25], such as the coulomb counting method, the open-circuit-voltage (OCV) method, the extended Kalman filter (EKF), fuzzy logic and the support vector machine [26], the proportional-integral (PI) observer [27], the Luenberger observer [28], the sliding mode observer [29] and the non-linear observers, multivariate adaptive regression splines [30], and bi-linear interpolation [31]. As the EKF is an optimum adaptive algorithm based on recursive estimation, it has attracted much attention [32]. However, the operation of the EKF assumes a Gaussian error distribution and the algorithm is inapplicable when the error distribution is non-Gaussian. In addition, as the EKF is based on ECM, the uncertainty of the ECM model parameters should be taken into consideration.

Previous studies have focused on the model parameter identification and the SOC estimation in a fixed range, little attention has been paid to the SOC estimation in the all SOC range (0–100%). In fact, the performance of the LIB in the all-region SOC is different. If the fixed model parameters are used for SOC estimation, the model error and SOC error may be very large. Moreover, Reference [33] confirmed that the model error of ECMs in the low SOC range (<20%) is much greater than that in the high SOC range, resulting in a large SOC estimation error based on the traditional EKF in the low SOC range. Therefore, it is necessary to develop an algorithm that can accurately estimate SOC in the low SOC range. In this study, an all-region model parameters identification method is proposed, and then a SOC estimator based on an improved EKF is developed to improve the accuracy of the SOC estimation in the all SOC range.

1.2. Main Contributions

This paper aims to develop a global parameter identification method and an all-region SOC estimator for the ECM. Specifically, the main contribution of this study is summarized as:

- (1) A subregion identification method for model parameter of ECMs in the all-region SOC is proposed to improve the global model accuracy. In this method, the all-region SOC (0–100%) is divided into several subregions, and the parameters in each subregion are identified. Therefore, the model parameter of the all-region is composed of the model parameter of each subregion. Moreover, the optimal number of subregions is investigated to balance the model accuracy and computation time.
- (2) An improved EKF-based SOC estimator with varying noise covariance is proposed to improve the accuracy of the SOC estimation in the all SOC range. ECM has a low model accuracy in the low SOC range, resulting in a large SOC estimation error based on the traditional EKF. The effectiveness of the proposed estimator in the all-region SOC is verified by experiments.
- (3) Our proposed model parameter identification method and SOC estimator are evaluated by two kinds of batteries under three working cycles.

1.3. Organization of the Paper

The rest of this paper is structured as follows: Section 2 describes the experimental equipment and results. In Section 3, a novel model-parameter identification method in the all SOC range is proposed. Section 4 describes an improved EKF-based SOC estimator. In Section 5, case studies of two kinds of batteries under three working cycles are employed to verify the effectiveness of the presented method and algorithm. Finally, conclusions are summarized in Section 6.

2. Experiment

The schematic of the test bench is shown in Figure 1a. It consists of a battery tester made by DIGATRON (BTS-600) (Digatron Power Electronics, Aachen, Germany), a thermal chamber for environment control and a host computer for operation control and data display/storage. The battery tester can charge/discharge a battery according to the designed program in a software installed on the host computer. The errors of the current and voltage sensors are less than 0.1%. The measured data and control command are transmitted to the host computer through the TCP/IP protocol. The acquired data are used to determine model parameters and verify the proposed SOC estimator.

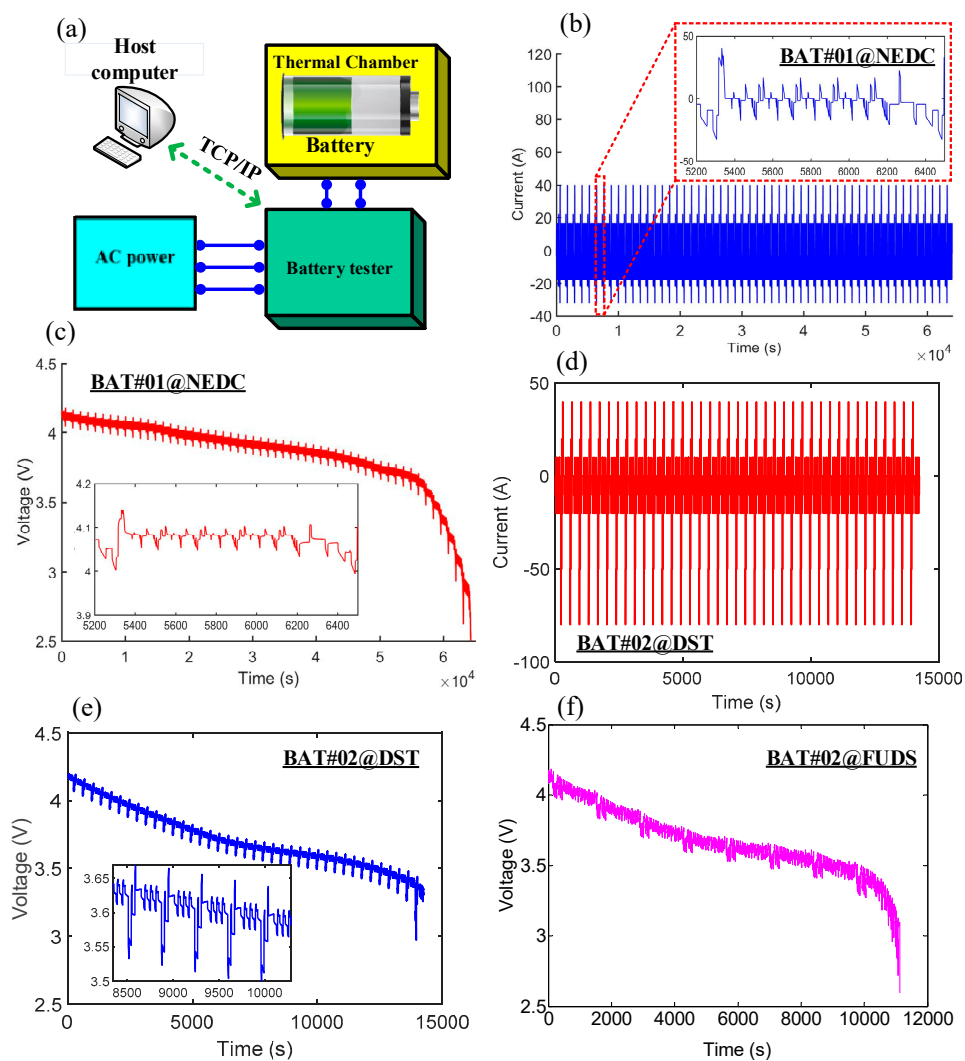


Figure 1. Battery test bench and experimental results under three working cycles. (a) Schematic of the test bench; (b) Current profile under the new European driving cycle (NEDC); (c) Voltage profile under the NEDC; (d) Current profile under the dynamic stress test (DST); (e) Voltage profile under the DST; (f) Voltage profile under the federal urban driving schedule (FUDS).

In order to fully verify the effectiveness of the proposed model identification method and SOC estimator, two types of batteries under three working cycles were selected for experiments. The main parameters of the two batteries are listed in Table 1. The experimental batteries were first fully charged and then discharged to the cut-off voltage under three working cycles, namely the new European driving cycle (NEDC), dynamic stress test (DST) and federal urban driving schedule (FUDS). The current and voltage during discharge were recorded, as shown in Figure 1b–f.

Moreover, the actual capacities and OCV curves of the test LIBs were determined by the standard capacity and hybrid pulse power characterization (HPPC) experiments. These experimental procedures are standard processes, which can be found in References [34,35].

Table 1. Main parameters of experimental battery.

	Nominal Capacity (Ah)	Lower Cut-Off Voltage (V)	Upper Cut-Off Voltage (V)	Maximum Charge Current (A)
BAT#01	32.5	2.5	4.15	65
BAT#02	40	2.8	4.2	100

3. Model and Parameter Identification

3.1. Equivalent Circuit Model

Reference [10] examined eleven ECMs and concluded that the first- and second-order RC models have the best balance of accuracy and reliability. Therefore, the 2RC model is used as the battery model for the parameter identification and SOC estimation in the all SOC range in this paper.

The model structure of 2RC is illustrated in Figure 2. In Figure 2, R_0 is equivalent to the Ohmic resistance, U_{OCV} is the voltage source, R_1 and R_2 are the diffusion resistances, and C_1 and C_2 are diffusion capacitances. The terminal voltages of the two series-connected RC circuits are denoted by U_1 and U_2 , the current is denoted by I , and the terminal voltage is denoted by U_L .

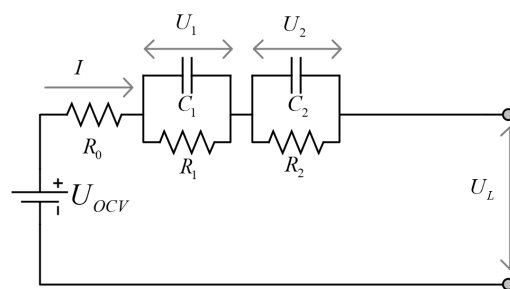


Figure 2. Model structure of 2RC.

Based on the circuit principle, the discretization equations of the 2RC model can be expressed as:

$$\begin{cases} U_L(k) = U_{OCV}(k) + I(k)R_0 + U_1(k) + U_2(k) \\ U_1(k+1) = U_1(k)e^{-\frac{\Delta t}{\tau_1}} + I(k)R_1 \left(1 - e^{-\frac{\Delta t}{\tau_1}}\right) \\ U_2(k+1) = U_2(k)e^{-\frac{\Delta t}{\tau_2}} + I(k)R_2 \left(1 - e^{-\frac{\Delta t}{\tau_2}}\right) \end{cases} \quad (1)$$

$$R_0 = \begin{cases} R_0^+ & i(k) \geq 0 \\ R_0^- & i(k) < 0 \end{cases} \quad (2)$$

where the subscript k denotes the time step, τ_1 and τ_2 are time constants of the RC network ($\tau_1 = R_1C_1$, $\tau_2 = R_2C_2$), Δt is the sampling period, and R_0^+ and R_0^- are the ohmic resistances during charging and discharging, respectively.

3.2. Model-Parameter Identification Based on Particle Swarm Optimization

To further improve the model accuracy, a suitable model parameter is essential. In the 2RC model, six parameters need to be determined, as is given in:

$$\theta = [R_0^+, R_0^-, \tau_1, R_1, \tau_2, R_2] \quad (3)$$

In this paper, the PSO algorithm is used to determine these model parameters in the all SOC range. The PSO algorithm is a global random search algorithm based on swarm intelligence, which simulates the migration and clustering behavior of birds in the process of foraging. The basic idea of the PSO is to find the optimal solution through cooperation and information sharing among individuals in the group [6,36–38]. The process of PSO can be briefly introduced as follows. In a D-dimensional search space, there are m particles. The position and velocity of the i -th particle ($1 \leq i \leq m$) can be expressed as $X_i = (X_{i1}, X_{i2}, \dots, X_{iD})$ and $V_i = (V_{i1}, V_{i2}, \dots, V_{iD})$, respectively. The best historical position of the i -th particle is expressed as $P_i = (P_{i1}, P_{i2}, \dots, P_{iD})$, and the best position for all particles is expressed as $P_g = (P_{g1}, P_{g2}, \dots, P_{gD})$. Then, particles update their speed and position according to the following expressions:

$$V_{iD}^{k+1} = \omega V_{iD}^k + c_1 r_1 (P_{iD}^k - X_{iD}^k) + c_2 r_2 (P_{gD}^k - X_{iD}^k) \quad (4)$$

$$X_{iD}^{k+1} = X_{iD}^k + V_{iD}^{k+1} \quad (5)$$

where ω is the inertia factor; k is the current iteration number; c_1 and c_2 are the acceleration constants; r_1 and r_2 are random numbers in range of (0, 1).

The pseudo codes of the PSO algorithm are listed in Algorithm 1. In the PSO, the root-mean-square-error (RMSE) between the model voltage and the measured voltage is used to establish the fitness function, which can be expressed as

$$M_{RMSE} = \sqrt{\frac{1}{n} \sum_{k=1}^n (u_k(\theta) - \hat{u}_k(\theta))^2} \quad (6)$$

where M_{RMSE} represents the RMSE of the battery model, u_k represents the model terminal voltage, and \hat{u}_k represents the measured voltage.

Algorithm 1. Pseudo-code of the PSO algorithm.

```

1: procedure PSO
2:   for each particle  $i$ 
3:     Initialize velocity  $V_i$  and position  $X_i$  for particle  $i$ 
4:     Evaluate particle  $i$  and set  $P_i = X_i$ 
5:   end for
6:    $gBest = \min [21]$ 
7:   while not stop
8:     for  $i = 1$  to  $n$ 
9:       Update the velocity and position of particle  $i$  using Equations (4) and (5)
10:      Evaluate particle  $i$ 
11:      if  $\text{fit}(X_i) < \text{fit}(P_i)$ 
12:         $P_i = X_i$ ;
13:      if  $\text{fit}(P_g) < \text{fit}(gBest)$ 
14:         $gBest = P_g$ ;
15:      end for
16:    end while
17: end procedure

```

3.3. All-Region Parameter Identification of ECM

Obviously, the nonlinearity of the external characteristics of the battery is very serious. Therefore, if fixed model parameters are used in the all SOC range, the model error is very large. In other words, the model parameters optimized by PSO in the all SOC range (constant model parameters are obtained) are the global optimum solution, but is not the best solution for each subregion. The reason is that the model parameters should be changed with SOC rather than being invariable. Therefore, a subregion identification method was developed to find the optimal solution of each subregion in this study (variable model parameters are obtained). The optimal solution of each subregion constitutes the best solution of the whole SOC range. In other words, the model with variable parameters has smaller model errors than that with constant parameters in the whole SOC range. The schematic of our proposed method is shown in Figure 3. The battery model used in this method is the 2RC model, which is introduced in detail in Section 3.1.

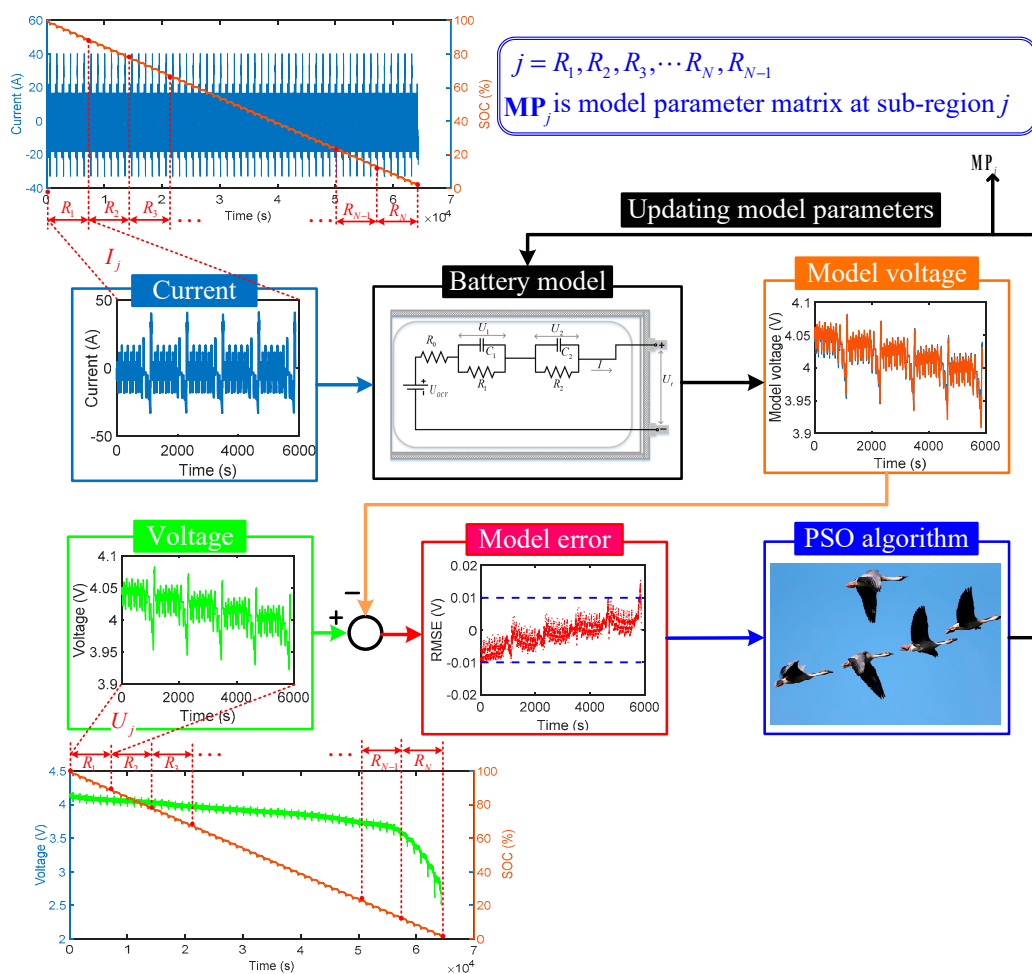


Figure 3. Framework of the parameter identification method of the equivalent circuit models (ECM) in the all state-of-charge (SOC) range.

The basic principle of the proposed method is as follows: the all SOC range (0–100%) is divided into N subregions, and the PSO algorithm is then used to identify the model parameters in each subregion. Therefore, N groups of model parameters are thereby obtained to form model parameters for the all SOC range. For the SOC estimation, the model parameters are selected based on the corresponding SOC range. This method of solving the optimal solution in each subregion to form the all-region solution can improve the accuracy of the model and lay a foundation for the accurate estimation of SOC. It should be noted that the real SOC is very difficult to obtain, so it is difficult to

accurately determine the SOC in each subregion, possibly resulting in the model parameters having errors. However, the model parameters are slow-varying and varied little in a small range. Therefore, the small model parameter error has little effect on the SOC estimation error. The flow of our method is as follows: firstly, the current SOC is obtained by the OCV-SOC curve, then the model parameters are obtained by judging the area in which the SOC is located. Finally, the SOC estimation is performed using our proposed estimator. Generally speaking, the SOC value obtained by the OCV-SOC curve may have an error, but the error is not very large. Therefore, the error of the model parameters obtained by our method is very small, and it is reasonable to use the SOC with a small error to query the model parameters.

As shown in Figure 3, the parameter identification process in each subregion is as follows. The input signal is the current, and the output signal of ECM is the model voltage based on the current model parameters. Then, the model error is obtained by comparing model voltage with measured voltage. Finally, model parameters are updated to pursue the minimum model error using PSO. When the optimal model parameters of the current subregion are identified, the optimal model parameters of the next subregion are solved until the model parameters of all regions are identified.

Obviously, the identification results are closely related to the value of the number of subregions (N). In order to investigate the relationship between model error, identification time and N values, we identified the model parameters under different N values. The identification process was run in MATLAB 2014b installed on a PC with 3.1 GHz CPU (Intel, Santa Clara, CA, USA) and 8 GB RAM (Kingston, Fountain Valley, CA, USA). The identification results are shown in Figures 4 and 5. Figure 4a shows the relationship between the RMSE and N under NEDC. It can be seen that the model error decreases with an increase in the value of N . However, the model error does not always decrease. When N is greater than 20, the model error will no longer decrease or even increase. Figure 4b shows the identification time under different N values. It can be seen that the identification time decreases with an increase in the value of N . The reason for this phenomenon can be expressed as follows: when N is small, the PSO algorithm takes a long time to find the optimal value in each subregion. When N is large, it is relatively easy for PSO to find the optimal solution. Therefore, the identification time becomes shorter. However, when N is greater than 20, the identification time is no longer reduced.

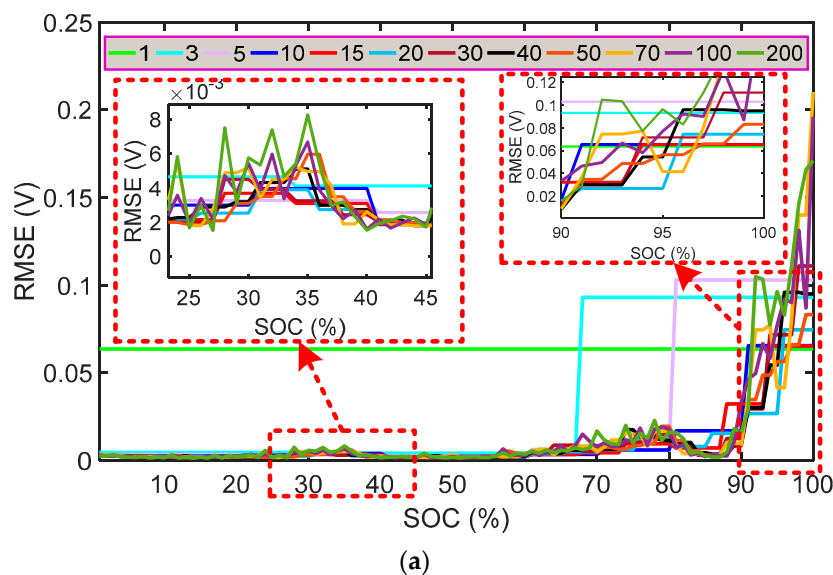


Figure 4. Cont.

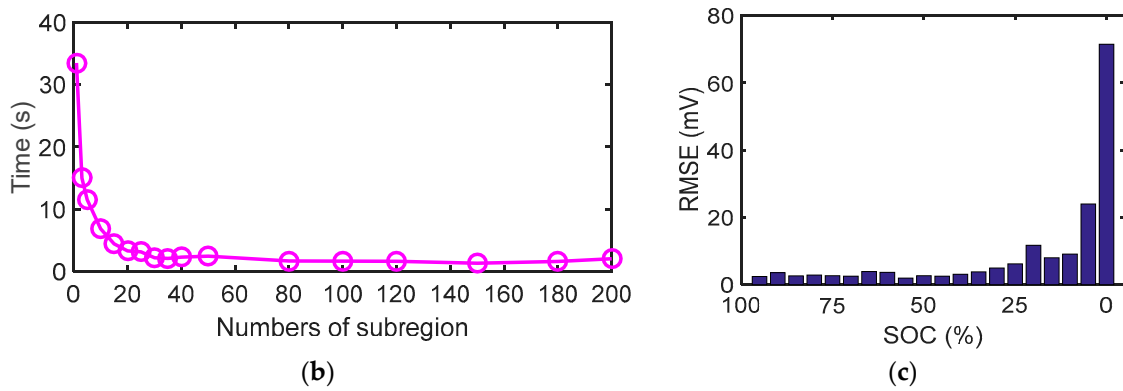


Figure 4. Identification results of BAT#01 under the new European driving cycle (NEDC). (a) Root-mean-square-error (*RMSE*) of the equivalent circuit models (ECM) under different *N* values. (b) Identification time under different *N* values. (c) Distribution of *RMSE* (*N* = 20).

To further clarify the relationship between model errors and the number of subregions, the parameter identification of another battery (BAT#02) under the DST and FUDS working cycles was carried out, and the identification results are shown in Figure 5. In Figure 5, the average *RMSE* is the average value of the *RMSE* of ECMs in the all SOC range. It can be seen that *N* = 20 is the best choice to balance the identification accuracy and the identification time under the DST and FUDS.

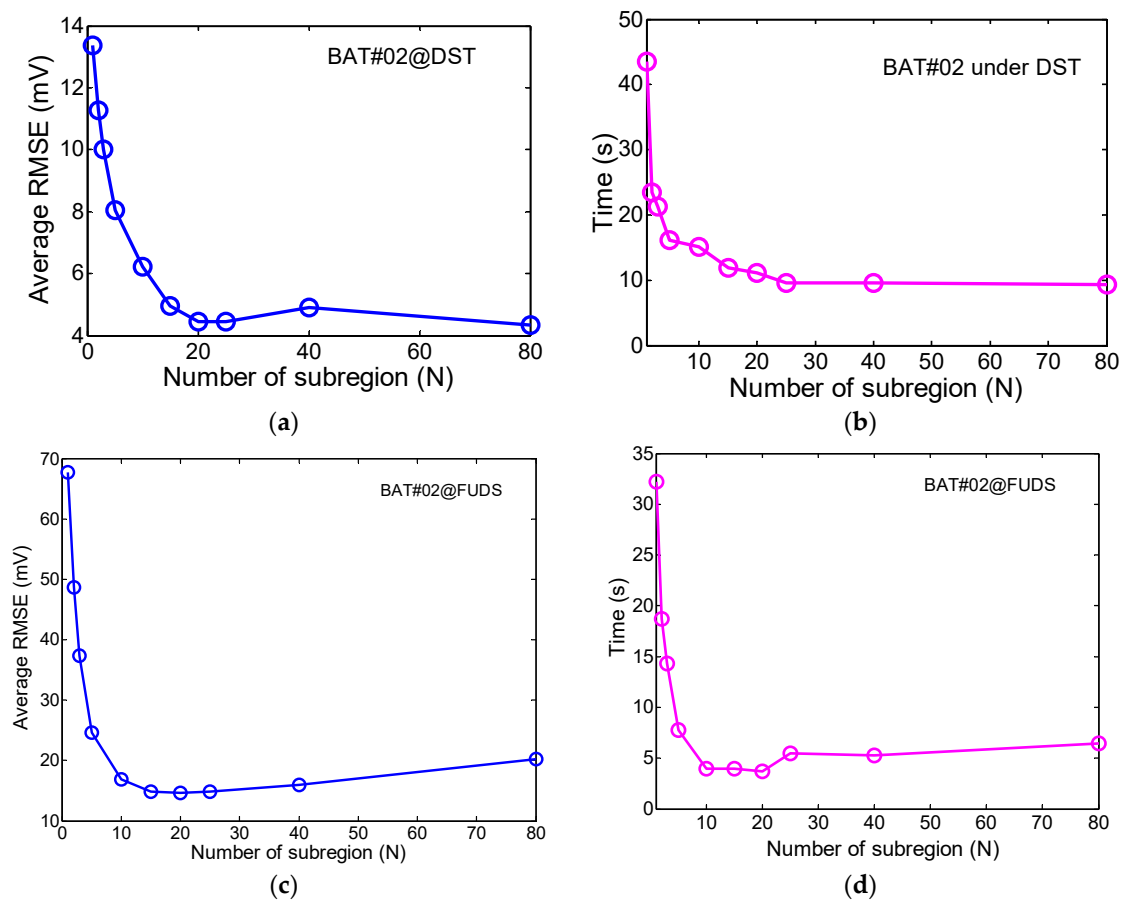


Figure 5. Identification results of BAT#02 under the dynamic stress test (DST) and the federal urban driving schedule (FUDS). (a) Relationship between average root-mean-square-error (*RMSE*) and *N* under the DST; (b) Relationship between identification time and *N* under the DST; (c) Relationship between average *RMSE* and *N* under the FUDS; (d) Relationship between identification time and *N* under the FUDS.

Based on the identification results of the above three working cycles, we can conclude that $N = 20$ is the best choice with the highest accuracy and the shortest identification time. Figure 4b shows the distribution of RMSE in the all SOC range ($N = 20$). It can be seen that the model has satisfactory accuracy in the high SOC range (20–100%), indicating the effectiveness of the proposed method. Table 2 lists the identification results of model parameters in the all SOC range. Note that the model error in the low SOC range (0–20%) is large, which is caused by the defects of the ECM. Therefore, model errors in the low SOC range need to be considered for an all-region SOC estimator.

Table 2. Identified parameters in all state-of-charge (SOC) range ($N = 20$).

SOC Range (%)	$R_0^+(\Omega)$	$R_0^-(\Omega)$	$R_1(\Omega)$	$\tau_1(s)$	$R_2(\Omega)$	$\tau_2(s)$
0–5	0.00151	0.00150	0.000802	25.96175	5.35×10^{-11}	910.1351
5–10	0.00142	0.00149	0.000144	4.291183	0.00089	36.14319
10–15	0.00128	0.00155	0.000428	7.268605	0.001204	76.50539
15–20	0.00142	0.00162	0.001829	292.5856	0.000979	26.74074
20–25	0.00130	0.00153	0.000559	11.88647	0.002403	149.2718
25–30	0.00136	0.00165	0.000891	29.3174	0.004348	725.8318
30–35	0.00137	0.00167	0.003932	493.7445	0.00058	18.99163
35–40	0.00139	0.00163	0.000674	23.38255	0.001858	363.3004
40–45	0.00130	0.00155	0.000478	12.50162	0.001385	152.1977
45–50	0.00118	0.00161	0.001177	172.2351	0.000491	11.14567
50–55	0.00139	0.00157	0.000675	23.54001	0.001762	262.7994
55–60	0.00143	0.00162	0.003075	609.9358	0.000921	37.09781
60–65	0.00132	0.00174	0.000826	34.21432	0.005307	862.0298
65–70	0.00130	0.00177	0.008134	766.7005	0.00057	18.45616
70–75	0.00144	0.00171	0.011066	934.3178	0.000646	23.98743
75–80	0.00130	0.00177	0.000409	8.049046	0.012025	788.1887
80–85	0.00133	0.00184	0.003062	377.0807	0.000918	32.84381
85–90	0.00169	0.00176	1.93×10^{-11}	307.087	0.016334	1000
90–95	0.00200	0.00168	0.067043	1000	0.003688	999.9995
95–100	0.00200	0.00200	0.082935	1000	0.064369	999.9998

4. An Improved EKF-Based SOC Estimator in the All SOC Range

4.1. EKF-Based SOC Estimator

The EKF is robust against modeling uncertainty, linearization error, and process and measurement noise. Therefore, the EKF is very suitable for the SOC estimation of LIBs. The schematic of the EKF-based SOC estimator is shown in Figure 6.

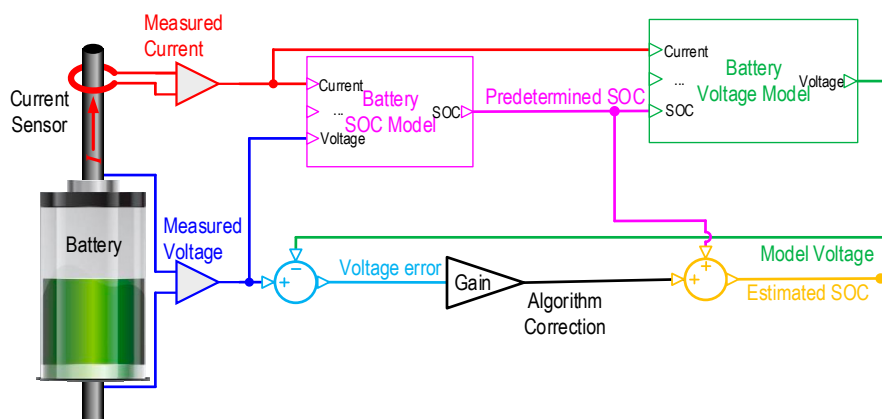


Figure 6. Schematic of the extended Kalman filter (EKF)-based state-of-charge (SOC) estimator.

For the 2RC model, the state variable x can be written as:

$$x = [SOC, U_1, U_2]^T \tag{7}$$

From Equations (2)–(4), the following expressions can be obtained:

$$f(x_k, u_k) = \begin{bmatrix} 1 & 0 & 0 \\ 0 & \exp(-\Delta t/\tau_1) & 0 \\ 0 & 0 & \exp(-\Delta t/\tau_2) \end{bmatrix} \begin{bmatrix} SOC_{EKF,k} \\ U_{1,k} \\ U_{2,k} \end{bmatrix} + \begin{bmatrix} -\eta\Delta t/C_n \\ R_1(1 - \exp(-\Delta t/\tau_1)) \\ R_2(1 - \exp(-\Delta t/\tau_2)) \end{bmatrix} I_k \tag{8}$$

$$g(x_k, u_k) = U_{OCV}(SOC_{EKF,k}) - I_k R_0 - U_{1,k} - U_{2,k} \tag{9}$$

where Δt is the sample period.

According to References [39,40], the standard EKF equations for the battery system are listed in Algorithm 2. Note that the Kalman gain L_k^x mainly depends on the comparison between the input noise covariance Σ_w and the output noise covariance Σ_v , thus choosing these two noise covariances properly has a great influence on the accuracy of the SOC estimation.

Algorithm 2. Summary of the extended Kalman filter (EKF)-based state-of-charge (SOC) estimator.

1: **Definitions:**

2: **The nonlinear state-space model:**

$$\begin{cases} x_{k+1} = f(x_k, u_k) + w_k \\ y_k = g(x_k, u_k) + v_k \end{cases}$$

where x is the system state vector, $f(x_k, u_k)$ is a state transition function and $g(x_k, u_k)$ is a measurement function, w_k is the unmeasured process noise and v_k is the measurement noise.

3: **Initialization:**

$$\hat{x}_0^+ = E[\hat{x}_0], \Sigma_{x,0}^+ = E[(x_0 - \hat{x}_0^+)(x_0 - \hat{x}_0^+)^T]$$

4: **Computation:**

5: **Time update:**

$$\hat{x}_k^- = f(\hat{x}_{k-1}^+, u_{k-1}) + \mathbf{w}_{k-1}; \Sigma_{x,k}^- = \mathbf{A}_{k-1} \Sigma_{x,k-1}^+ \mathbf{A}_{k-1}^T + \Sigma_w$$

7: **Measurement update:**

8: Error innovation: $e_k = y_k - \hat{y}_k = y_k - g(\hat{x}_k^-, u_k)$.

9: Estimator gain matrix: $L_k^x = \Sigma_{x,k}^- (\mathbf{C}_k^x)^T [\mathbf{C}_k^x \Sigma_{x,k}^- \mathbf{C}_k^x + \Sigma_v]^{-1}$

10: Measurement update: $\hat{x}_k^+ = \hat{x}_k^- + L_k^x [y_k - \hat{y}_k]$

11: Error covariance measurement update: $\Sigma_{x,k}^+ = (\mathbf{I} - L_k^x \mathbf{C}_k^x) \Sigma_{x,k}^-$

where $\mathbf{A}_k = \left. \frac{\partial f(x_k, u_k)}{\partial x} \right|_{x=\hat{x}_k^+}$, $\mathbf{C}_k = \left. \frac{\partial g(x_k, u_k)}{\partial x} \right|_{x=\hat{x}_k^-}$

4.2. An Improved EKF-Based SOC Estimator

Section 3.3 indicates that the ECM has low accuracy in the low SOC range. Therefore, the SOC error obtained by the traditional EKF is large. To solve this problem, an improved EKF (IEKF)-based SOC estimator is proposed in this paper. The expression of L_k^x , the relative ratio of Σ_w and Σ_v , determines the performance of the EKF algorithm. Figure 7 shows the SOC and SOC error based on the EKF with different distributions of noise covariance under the NEDC, FUDS and DST working cycles (capacity error is set to 0.5%). The calculation results of the three working cycles show that the SOC estimated value is more inclined to the SOC value obtained by the ampere-hour (AH) method when the Σ_w is smaller and the Σ_v is larger, while the estimated value is more inclined to the SOC estimated value obtained by the normal EKF when the Σ_w is larger and the Σ_v is smaller. As shown in Figure 4a, the model error is very large in the low SOC range, resulting in a large SOC estimation error based on the traditional EKF. At this time, the SOC estimation value obtained by the AH method is more reliable, because the AH method is not affected by the ECM error. Therefore, a smaller Σ_w value

and a larger Σ_v value should be used. When the model error is small, it indicates that the battery is in the high SOC range, and Σ_w and Σ_v should return to the normal value.

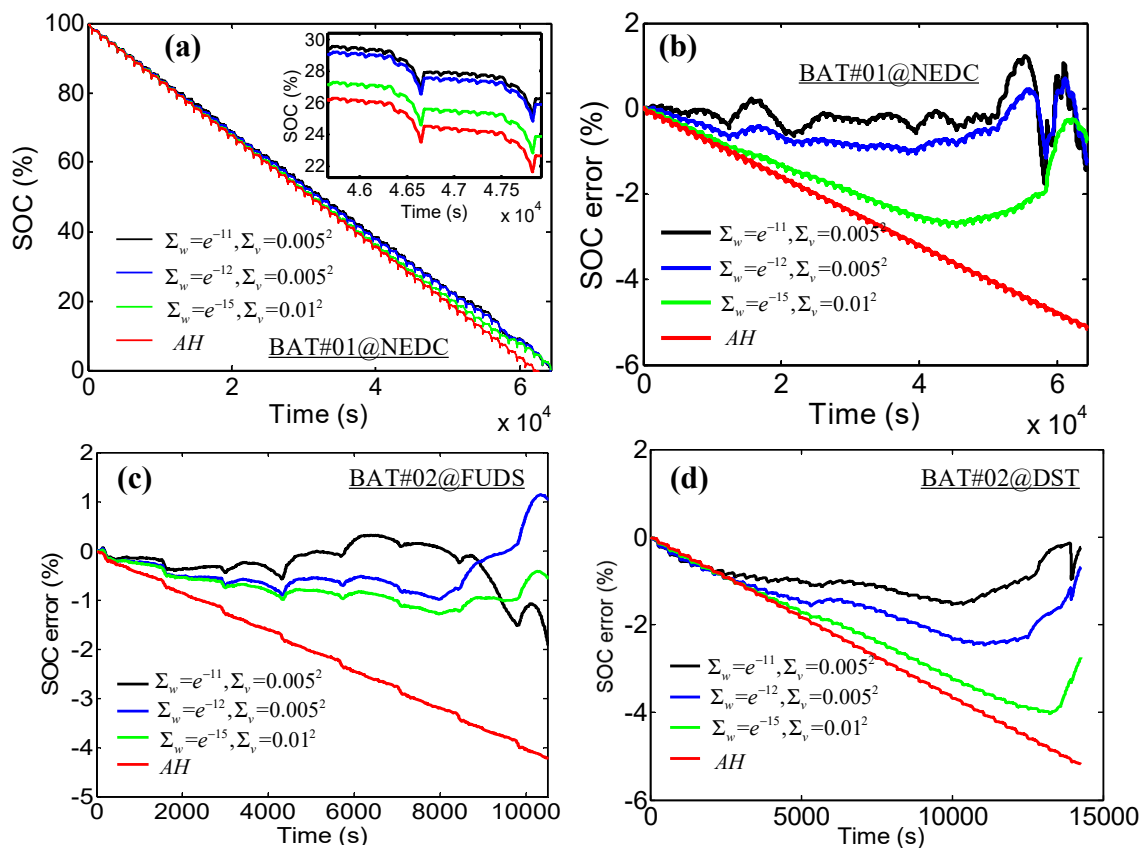


Figure 7. State-of-charge (SOC) and SOC error based on the extended Kalman filter (EKF) with different distributions of noise covariance under three working cycles (capacity error is set to 0.5%). (a) SOC of BAT#01 under the new European driving cycle (NEDC); (b) SOC error of BAT#01 under NEDC; (c) SOC error of BAT#02 under the federal urban driving schedule (FUDS); (d) SOC error of BAT#02 under the dynamic stress test (DST).

When the accuracy of the ECM is insufficient in the low SOC range, the IEKF algorithm is more confident in the estimation value using the AH method. Therefore, the accuracy of the AH method directly affects the SOC estimation accuracy in the low SOC range. The error sources of the AH method include capacity error, coulombic efficiency error, measured current error, self-discharge etc. The specific influence of these factors on the AH method is as follows.

- (a) Case 1: the capacity error is 5%. Figure 8 shows that the maximum incremental error of the SOC caused by the AH method in this case is 1% in the low SOC range (0–20%).
- (b) Case 2: the coulomb efficiency error is 0.1%. Figure 8 shows that the maximum incremental error caused by the AH method in this case is 0.1% in the low SOC range.
- (c) Case 3: the drift of the measured current is 100 mA, and the self-discharge is 1 mA. Figure 8 shows that the maximum incremental error in this case is less than 1%.

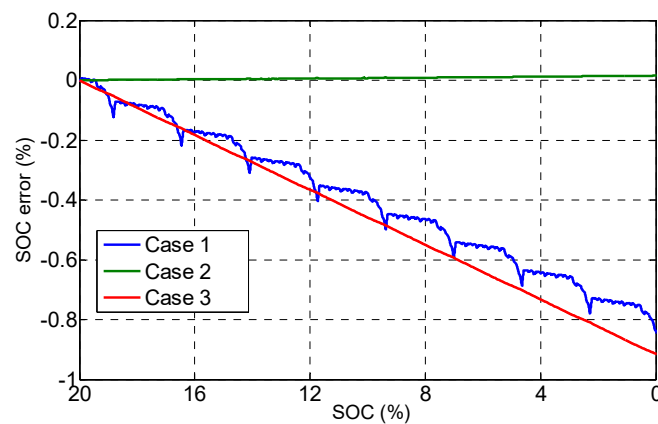


Figure 8. Calculation of the state-of-change (SOC) error source based on the ampere-hour (AH) method.

In summary, the maximum incremental error caused by the AH method cannot exceed 2.0% in the all low SOC range even if the above assumptions are superimposed. Therefore, our proposed method is useful for improving the accuracy of SOC estimation in low SOC range.

However, the exact Kalman noise covariance cannot be directly obtained. In this paper, we take the model error (M_{RMSE}) as the reference signal. The model error is obtained by comparing the measured voltage with the one obtained by the model. From Section 3.3, we can see that the low SOC range is 20% of the all-region SOC. Therefore, the cumulative error caused by the AH method is small, and once the normal EKF algorithm is returned, the initial error can be eliminated. The values of Σ_w and Σ_v are listed in Equation (10). The proposed method improves the SOC estimation accuracy in the all SOC range by adjusting the distribution of noise covariance according to the model error in real time.

$$(\Sigma_w, \Sigma_v) = \begin{cases} (e^{-11}, 0.005^2) & M_{RMSE} \leq 0.003V \\ (e^{-12}, 0.005^2) & 0.003V < M_{RMSE} \leq 0.006V \\ (1e^{-15}, 0.010^2) & 0.006V < M_{RMSE} \leq 0.009V \\ (e^{-50}, 1.000^2) & M_{RMSE} > 0.009V \end{cases} \quad (10)$$

5. Results and Discussion

5.1. Case Studies under NEDC

To verify the effectiveness of the proposed all-region model-parameter identification and SOC estimator, the SOC is estimated under various cases using the experimental data in Section 2. The estimated results are shown in Figure 9. Figure 9a shows the SOC estimation error in ideal conditions. In this paper, the ideal condition means there is no capacity error and sensor measurement error. The results indicate that the proposed IEKF algorithm has much higher accuracy in the low SOC range than the EKF algorithm, and has almost the same accuracy in the high SOC range. Figure 9b shows the SOC error is under 5% of the capacity error, indicates that the IEKF algorithm is better than EKF in the all SOC range. In practical applications, the errors of current sensor and voltage sensor exist. Figure 9c shows the SOC error of two algorithms under a current error of 32.5 mA noise and 32.5 mA drift (0.1% full scale of current sensor). Figure 9d shows the SOC error under a voltage error of 10 mV noise and 5 mV drift. Table 3 lists the RMSE of the SOC in the all SOC range. Case studies show that the SOC error obtained by EKF and IEKF is almost the same in the high SOC range ($SOC \geq 20\%$). However, the SOC error obtained by IEKF is obviously smaller than that by EKF in the low SOC range ($SOC < 20\%$). Figure 10 shows the SOC estimation result under NEDC in the all SOC range. It is obvious that the SOC obtained by the IEKF tracks the real SOC better than that obtained by the EKF. Moreover, our proposed IEKF only adjusts the distribution of noise covariance on the basis of the

traditional EKF. Therefore, the computation times of IEKF and EKF are almost the same. Through the above analysis, we can conclude that our proposed IEKF is better than the traditional EKF in the all SOC range.

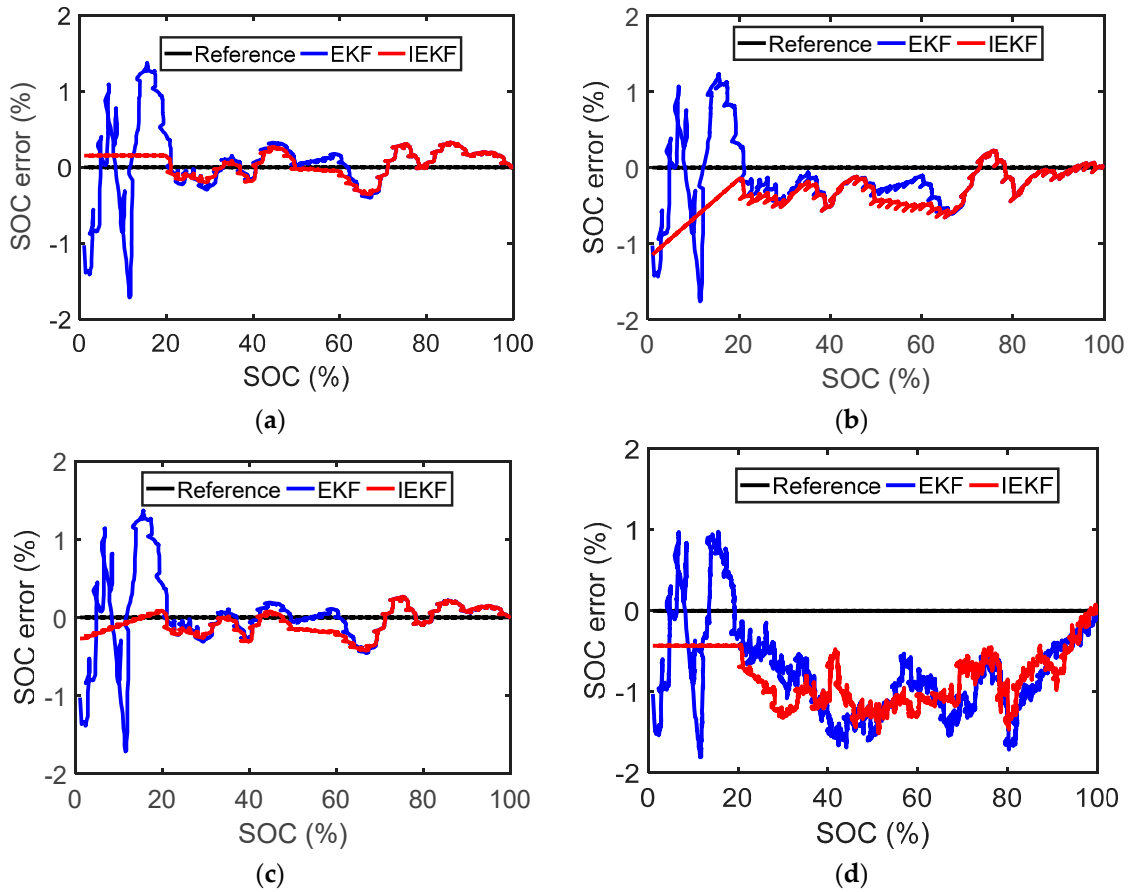


Figure 9. The state-of-charge (SOC) estimated error comparison in the all-region SOC under the new European driving cycle (NEDC). (a) Case A: SOC error in ideal condition; (b) Case B: SOC error under 5% capacity error; (c) Case C: SOC error under current error of 32.5 mA noise and 32.5 mA drift; (d) Case D: SOC error under voltage error of 10 mV noise and 5 mV drift.

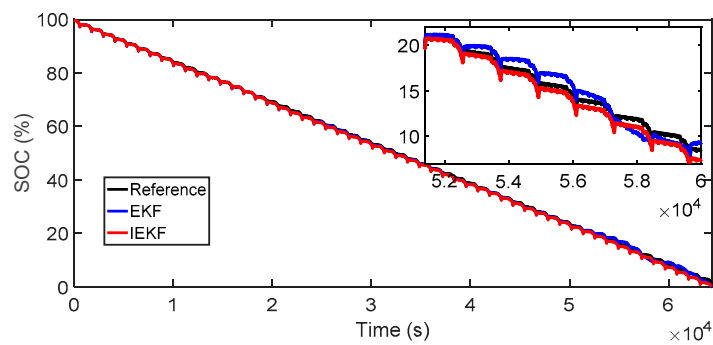


Figure 10. State-of-charge (SOC) estimation results under the new European driving cycle (NEDC) in the all-region SOC (capacity error is set to 6%, current error is 50 mA noise and 50 mA drift).

Table 3. Root-mean-square-error (RMSE) in the all state-of-charge (SOC) range.

Case	EKF	IEKF
Case A	0.43%	0.17%
Case B	0.44%	0.41%
Case C	0.57%	0.44%
Case D	1.47	1.25%

5.2. Additional Validation under the DST and FUDS Working Conditions

In order to further verify the reliability and accuracy of the proposed algorithm, verification on another battery (BAT#02) under the DST and FUDS is performed. The results are shown in Figure 11. It can be seen that the accuracy of our proposed IEKF is higher than that of EKF under the DST and FUDS in the all-region SOC.

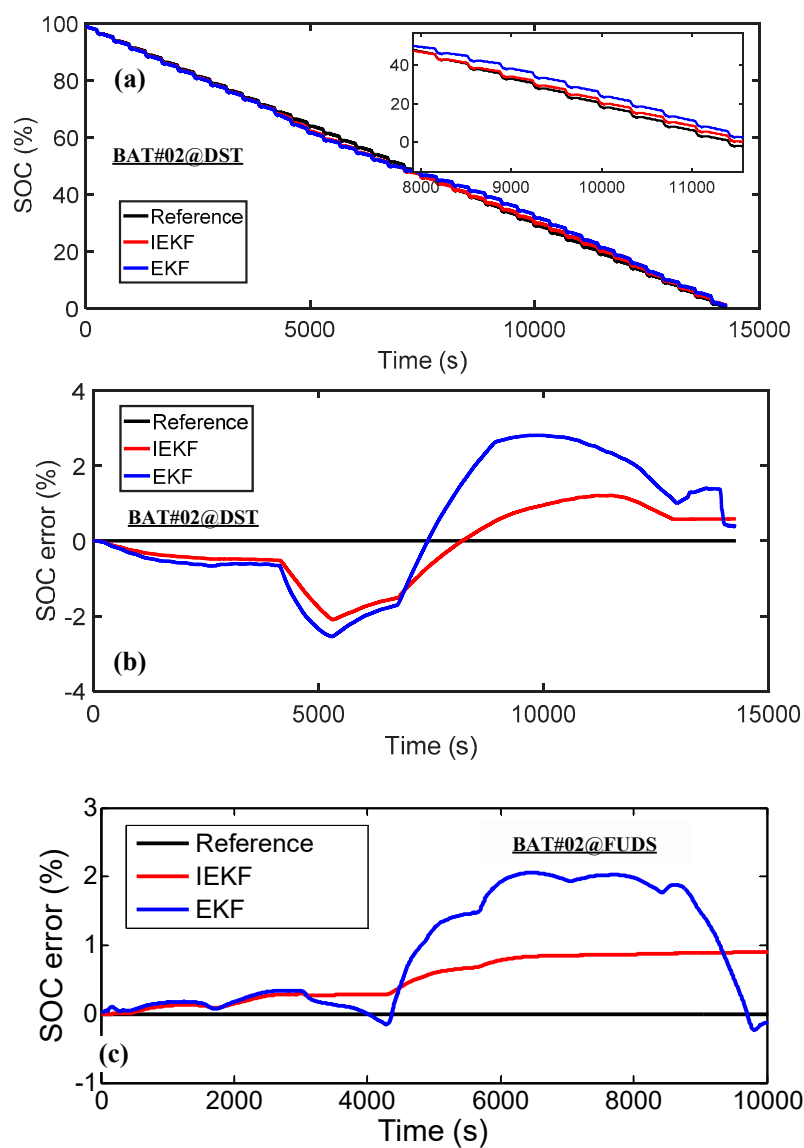


Figure 11. State-of-charge (SOC) estimation results of BAT#2 under the dynamic stress test (DST) and the federal urban driving schedule (FUDS) in the all SOC range. (a) SOC estimation value under the DST; (b) Estimation error under the DST; (c) Estimation error under the FUDS.

In conclusion, the effectiveness of the proposed parameter identification method and SOC estimator are verified by case studies under NEDC, DST and FUDS working conditions, and the accuracy and reliability of IEKF are better than traditional EKF in the all SOC range.

6. Conclusions

In this paper, a model parameter identification method was proposed to improve the global model accuracy for the ECM. Then, an improved EKF-based SOC estimator with varying noise covariance was developed to improve the SOC estimation accuracy in the low SOC range, which can solve the problem of a low estimation accuracy of traditional EKF based on the ECM in the low SOC range. The experimental results of two kinds of batteries under the NEDC and DST working cycles show that: (1) the proposed parameter identification method of ECM can achieve global optimum in the all SOC range, and the model error is within 10 mV when the SOC ranges from 100% to 20%. Moreover, the model accuracy does not always improve by increasing the number of subregions (N). Conversely, the model accuracy no longer increases or even decreases when N increases to a certain value. Our investigation shows that $N = 20$ is the best choice with the highest accuracy and the shortest identification time; (2) the SOC estimation error is within $\pm 1\%$ in the all SOC range, indicating that the proposed IEKF has better accuracy and reliability than the traditional EKF.

It should be noted that our proposed method and algorithm are only verified by experiments in the DST and NEDC working cycles. However, the results can provide valuable references for the battery model parameter identification and SOC estimation in real applications. The application of the proposed method and algorithm in real EVs will be our future research work.

Author Contributions: All authors contributed to the paper. Conceptualization, X.L. and Y.Z.; data curation, W.Y. and L.Z.; investigation, X.L.; methodology, X.L.; project administration, X.L. and Y.Z.; software, X.L.; validation, X.L.; writing (original draft), X.L. and W.Y.; writing (review and editing), X.L. and Y.Z.

Funding: This research was funded by the National Natural Science Foundation of China (NSFC) under the grant number of 51505290 and 51507102.

Conflicts of Interest: The authors declare no conflicts of interest.

References

1. Yang, D.; Zhang, X.; Pan, R.; Wang, Y.J.; Chen, Z.H. A novel gaussian process regression model for state-of-health estimation of lithium-ion battery using charging curve. *J. Power Sources* **2018**, *384*, 387–395. [[CrossRef](#)]
2. Lai, X.; Zheng, Y.J.; Zhou, L.; Gao, W.K. Electrical behavior of overdischarge-induced internal short circuit in lithium-ion cells. *Electrochim. Acta* **2018**, *278*, 245–254. [[CrossRef](#)]
3. Genc, R.; Alas, M.O.; Harputlu, E.; Repp, S.; Kremer, N.; Castellano, M.; Colak, S.G.; Ocakoglu, K.; Erdem, E. High-capacitance hybrid supercapacitor based on multi-colored fluorescent carbon-dots. *Sci. Rep.* **2017**, *7*, 11222. [[CrossRef](#)] [[PubMed](#)]
4. Garcia, J.; Garcia, P.; Giulii Capponi, F.; De Donato, G. Analysis, modeling, and control of half-bridge current-source converter for energy management of supercapacitor modules in traction applications. *Energies* **2018**, *11*, 2239. [[CrossRef](#)]
5. Repp, S.; Harputlu, E.; Gurgun, S.; Castellano, M.; Kremer, N.; Pompe, N.; Worner, J.; Hoffmann, A.; Thomann, R.; Emen, F.M.; et al. Synergetic effects of Fe³⁺ doped spinel Li₄Ti₅O₁₂ nanoparticles on reduced graphene oxide for high surface electrode hybrid supercapacitors. *Nanoscale* **2018**, *10*, 1877–1884. [[CrossRef](#)] [[PubMed](#)]
6. Xia, B.Z.; Cui, D.Y.; Sun, Z.; Lao, Z.Z.; Zhang, R.F.; Wang, W.; Sun, W.; Lai, Y.Z.; Wang, M.W. State of charge estimation of lithium-ion batteries using optimized levenberg-marquardt wavelet neural network. *Energy* **2018**, *153*, 694–705. [[CrossRef](#)]
7. Hu, X.S.; Zou, C.F.; Zhang, C.P.; Li, Y. Technological developments in batteries. *IEEE Power Energy Mag.* **2017**, *15*, 20–31. [[CrossRef](#)]

8. Lu, L.G.; Han, X.B.; Li, J.Q.; Hua, J.F.; Ouyang, M.G. A review on the key issues for lithium-ion battery management in electric vehicles. *J. Power Sources* **2013**, *226*, 272–288. [[CrossRef](#)]
9. Rivera-Barrera, J.P.; Munoz-Galeano, N.; Sarmiento-Maldonado, H.O. SOC estimation for lithium-ion batteries: Review and future challenges. *Electronics* **2017**, *6*, 102. [[CrossRef](#)]
10. Lai, X.; Zheng, Y.J.; Sun, T. A comparative study of different equivalent circuit models for estimating state-of-charge of lithium-ion batteries. *Electrochim. Acta* **2018**, *259*, 566–577. [[CrossRef](#)]
11. Zheng, L.F.; Zhu, J.G.; Lu, D.D.C.; Wang, G.X.; He, T.T. Incremental capacity analysis and differential voltage analysis based state of charge and capacity estimation for lithium-ion batteries. *Energy* **2018**, *150*, 759–769. [[CrossRef](#)]
12. Ungurean, L.; Carstoiu, G.; Micea, M.V.; Groza, V. Battery state of health estimation: A structured review of models, methods and commercial devices. *Int. J. Energy Res.* **2017**, *41*, 151–181. [[CrossRef](#)]
13. Shen, P.; Ouyang, M.G.; Lu, L.G.; Li, J.Q.; Feng, X.N. The co-estimation of state of charge, state of health, and state of function for lithium-ion batteries in electric vehicles. *IEEE Trans. Veh. Technol.* **2018**, *67*, 92–103. [[CrossRef](#)]
14. Zheng, Y.J.; Ouyang, M.G.; Han, X.B.; Lu, L.G.; Li, J.Q. Investigating the error sources of the online state of charge estimation methods for lithium-ion batteries in electric vehicles. *J. Power Sources* **2018**, *377*, 161–188. [[CrossRef](#)]
15. Xiong, R.; Cao, J.Y.; Yu, Q.Q.; He, H.W.; Sun, F.C. Critical review on the battery state of charge estimation methods for electric vehicles. *IEEE Access* **2018**, *6*, 1832–1843. [[CrossRef](#)]
16. Attidekou, P.S.; Lambert, S.; Armstrong, M.; Widmer, J.; Scott, K.; Christensen, P.A. A study of 40 ah lithium ion batteries at zero percent state of charge as a function of temperature. *J. Power Sources* **2014**, *269*, 694–703. [[CrossRef](#)]
17. Meng, J.H.; Luo, G.Z.; Ricco, M.; Swierczynski, M.; Stroe, D.I.; Teodorescu, R. Overview of lithium-ion battery modeling methods for state-of-charge estimation in electrical vehicles. *Appl. Sci.* **2018**, *8*, 659. [[CrossRef](#)]
18. Wang, T.P.; Chen, S.Z.; Ren, H.B.; Zhao, Y.Z. Model-based unscented kalman filter observer design for lithium-ion battery state of charge estimation. *Int. J. Energy Res.* **2018**, *42*, 1603–1614. [[CrossRef](#)]
19. Xing, Y.J.; He, W.; Pecht, M.; Tsui, K.L. State of charge estimation of lithium-ion batteries using the open-circuit voltage at various ambient temperatures. *Appl. Energy* **2014**, *113*, 106–115. [[CrossRef](#)]
20. Pei, Z.D.; Zhao, X.X.; Yuan, H.M.; Peng, Z.; Wu, L.F. An equivalent circuit model for lithium battery of electric vehicle considering self-healing characteristic. *J. Control Sci. Eng.* **2018**, *2018*, 5179758. [[CrossRef](#)]
21. Farmann, A.; Sauer, D.U. Comparative study of reduced order equivalent circuit models for on-board state-of-available-power prediction of lithium-ion batteries in electric vehicles. *Appl. Energy* **2018**, *225*, 1102–1122. [[CrossRef](#)]
22. Mesbahi, T.; Khenfri, F.; Rizoug, N.; Chaaban, K.; Bartholomeus, P.; Le Moigne, P. Dynamical modeling of Li-ion batteries for electric vehicle applications based on hybrid particle swarm-nelder-mead (PSO-NM) optimization algorithm. *Electr. Power Syst. Res.* **2016**, *131*, 195–204. [[CrossRef](#)]
23. Dai, H.F.; Xu, T.J.; Zhu, L.T.; Wei, X.Z.; Sun, Z.C. Adaptive model parameter identification for large capacity li-ion batteries on separated time scales. *Appl. Energy* **2016**, *184*, 119–131. [[CrossRef](#)]
24. Hu, X.; Sun, F.; Zou, Y. Comparison between two model-based algorithms for li-ion battery soc estimation in electric vehicles. *Simul. Model. Pract. Theory* **2013**, *34*, 1–11. [[CrossRef](#)]
25. Zou, Y.; Hu, X.; Ma, H.; Li, S.E. Combined state of charge and state of health estimation over lithium-ion battery cell cycle lifespan for electric vehicles. *J. Power Sources* **2015**, *273*, 793–803. [[CrossRef](#)]
26. Wu, X.; Mi, L.; Tan, W.; Qin, J.L.; Zhao, M.N. State of charge (SOC) estimation of Ni-MH battery based on least square support vector machines. *Adv. Mater. Res.* **2011**, *211–212*, 1204–1209. [[CrossRef](#)]
27. Xu, J.; Mi, C.C.; Cao, B.G.; Deng, J.J.; Chen, Z.; Li, S.Q. The state of charge estimation of lithium-Ion batteries based on a proportional-integral observer. *IEEE Trans. Veh. Technol.* **2014**, *63*, 1614–1621.
28. Li, J.H.; Barillas, J.K.; Guenther, C.; Danzer, M.A. A comparative study of state of charge estimation algorithms for LiFePO₄ batteries used in electric vehicles. *J. Power Sources* **2013**, *230*, 244–250. [[CrossRef](#)]
29. Chen, X.P.; Shen, W.X.; Cao, Z.W.; Kapoor, A. A novel approach for state of charge estimation based on adaptive switching gain sliding mode observer in electric vehicles. *J. Power Sources* **2014**, *246*, 667–678. [[CrossRef](#)]
30. Anton, J.C.A.; Nieto, P.J.G.; Juez, F.J.D.; Lasheras, F.S.; Viejo, C.B.; Gutierrez, N.R. Battery state-of-charge estimator using the mars technique. *IEEE Trans. Power Electr.* **2013**, *28*, 3798–3805. [[CrossRef](#)]

31. Wang, L.Y.; Wang, L.F.; Li, Y. A novel state-of-charge estimation algorithm of EV battery based on bilinear interpolation. In *Proceedings of the 2013 9th IEEE Vehicle Power and Propulsion Conference (VPPC)*; IEEE: New York, NY, USA, 2013; pp. 26–29.
32. Barillas, J.K.; Li, J.H.; Gunther, C.; Danzer, M.A. A comparative study and validation of state estimation algorithms for Li-ion batteries in battery management systems. *Appl. Energy* **2015**, *155*, 455–462. [[CrossRef](#)]
33. Ouyang, M.G.; Liu, G.M.; Lu, L.G.; Li, J.Q.; Han, X.B. Enhancing the estimation accuracy in low state-of-charge area: A novel onboard battery model through surface state of charge determination. *J. Power Sources* **2014**, *270*, 221–237. [[CrossRef](#)]
34. Lai, X.; Qiao, D.; Zheng, Y.; Zhou, L. A fuzzy state-of-charge estimation algorithm combining ampere-hour and an extended kalman filter for Li-ion batteries based on multi-model global identification. *Appl. Sci.* **2018**, *8*, 2028. [[CrossRef](#)]
35. Xin Lai, C.Q.; Gao, W.; Zheng, Y.; Yi, W. A state of charge estimator based extended kalman filter using an electrochemistry-based equivalent circuit model for lithium-ion batteries. *Appl. Sci.* **2018**, *8*, 1592.
36. Wang, S.C.; Liu, Y.H. A pso-based fuzzy-controlled searching for the optimal charge pattern of Li-ion batteries. *IEEE Trans. Ind. Electron.* **2015**, *62*, 2983–2993. [[CrossRef](#)]
37. Anton, J.C.A.; Nieto, P.J.G.; Gonzalo, E.G.; Perez, J.C.V.; Vega, M.G.; Viejo, C.B. A new predictive model for the state-of-charge of a high-power lithium-ion cell based on a PSO-optimized multivariate adaptive regression spline approach. *IEEE Trans. Veh. Technol.* **2016**, *65*, 4197–4208. [[CrossRef](#)]
38. Kermadi, M.; Berkouk, E. A maximum power point tracker based on particle swarm optimization for pv-battery energy system under partial shading conditions. In *Proceedings of the 3rd International Conference on Control, Engineering & Information Technology (Ceit 2015)*, Tlemcen, Algeria, 25–27 May 2015.
39. Wei, J.; Dong, G.; Chen, Z.; Kang, Y. System state estimation and optimal energy control framework for multicell lithium-ion battery system. *Appl. Energy* **2017**, *187*, 37–49. [[CrossRef](#)]
40. Gao, W.; Zheng, Y.; Ouyang, M.; Li, J.; Lai, X.; Hu, X. Micro-short circuit diagnosis for series-connected lithium-ion battery packs using mean-difference model. *IEEE Trans. Ind. Electron.* **2019**, *66*, 2132–2142. [[CrossRef](#)]



© 2018 by the authors. Licensee MDPI, Basel, Switzerland. This article is an open access article distributed under the terms and conditions of the Creative Commons Attribution (CC BY) license (<http://creativecommons.org/licenses/by/4.0/>).